Anomalous Vibrational Modes in Few Layer WTe2 Revealed by Polarized

Raman Scattering and First-Principles Calculations

- 3 Yan Cao^{1,&}, Natalya Sheremetyeva^{2,&}, Liangbo Liang³, Hui Yuan¹, Tingting Zhong¹, Vincent
- 4 Meunier^{2*} and Minghu Pan^{1*}
- ¹ School of Physics, Huazhong University of Science and Technology, Wuhan 430074, China.
- 6 ² Department of Physics, Applied Physics and Astronomy, Rensselaer Polytechnic Institute, Troy,
- 7 NY 12180, USA.
- 8 ³ Center for Nanophase Materials Sciences, Oak Ridge National Laboratory, Oak Ridge, TN 37831,
- 9 USA.

10

15

16

17

18

19

20

21

22

23

24

25

26

27

28

29

1

2

- 11 &These authors contributed equally to this work.
- *To whom correspondence should be addressed. M. H. Pan [minghupan@hust.edu.cn] and V.
- 13 Meunier [meuniv@rpi.edu]
- 14 **KEYWORDS:** transition-metal dichalcogenide, WTe₂, Raman Spectrum, DFT

When layered transition-metal dichalcogenides (TMDs) are scaled down from a threeto a two-dimensional geometry, electronic and structural transitions occur, leading to the
emergence of properties not usually found in the bulk. Here, we report a systematic
Raman study of exfoliated semi-metallic WTe₂ flakes with thickness ranging from few
layers down to a single layer. A dramatic change in the Raman spectra occurs between the
monolayer and few-layer WTe₂ as a vibrational mode centered at ~86.9 cm⁻¹ in the
monolayer splits into two active modes at 82.9 and 89.6 cm⁻¹ in the bilayer. Davydov
splitting of these two modes is found in the bilayer, as further evidenced by polarized
Raman measurements. Strong angular dependence of Raman modes on the WTe₂ film
thickness reflects that the existence of directional interlayer interaction, rather than
isotropic van der Waals (vdw) coupling, is playing an essential role affecting the phonon
modes, especially in anisotropic 2D WTe₂ material. Therefore, the strong evolution of
Raman modes with thickness and polarization direction, can not only be a reliable
fingerprint for the determination of the thickness and the crystallographic orientation, but
can also be an ideal probe for such strong and directional interlayer interaction.

1 1. Introduction

2 Interlayer interactions play a critical role in determining the physical properties of transition-3 metal dichalcogenides (TMDs), as they affect the layered structure, the interlayer electronic bands and the atomic vibrations. The physical properties of TMDs are greatly dependent on the 4 number of layers¹⁻³. For example, the variation of properties reveals a thickness dependence of 5 Raman frequency shifts away from the bulk 4, 5. Further, when a TMD is scaled down to a single 6 7 atomic layer, the material converts into a unique form of matter, where the electronic and optical 8 properties can change dramatically although the chemical content and stoichiometry are not 9 changed⁶. Anisotropic layered TMD WTe2, whose sheets consist of a tungsten layer sandwiched between 10 chalcogenide layers, has been the subject of intense interest owing to its extraordinary 11 magnetoresistance (XMR)⁷. Recent results show that WTe₂ features a complicated Fermi surface⁸ 12 13 and circular dichroism experiments further confirm the existence of a spin texture at the Fermi 14 surface in photoemission spectra⁹. Recently, WTe₂ was proposed as the first T_d-TMDs to host type II Weyl fermions, as it features intriguing band topology with Weyl points of opposite chirality¹⁰. 15 16 This has led to significant research efforts aimed at revealing WTe₂'s rich fundamental properties 17 related to superconductivity, electronic band structure, Fermi surface, lattice vibrations, charge 18 transport, etc. 19 Generally, TMDs can adopt a number of structural configurations, including the 2H, 1T, 1T' and 20 T_d structures. WTe₂ is a metal usually found in the stable T_d structure (orthorhombic structure, 21 space group Pnm21)¹¹. In contrast, many other TMDs are usually semiconductors featuring 2H (hexagonal, space group P63/mmc) or 1T symmetries. Our studies show that the WTe₂ structure 22 23 undergoes a dramatic phase change when the thickness is varied from the monolayer regime to 24 few-layer configurations. 25 Raman scattering has proven to be one of the most adequate techniques for studying twodimensional materials, especially TMDs as it enables the determination of the structure and 26 number of layers in a nondestructive way¹². In particular, Raman reveals crucial information on 27 28 the weak interlayer interaction that causes the splitting of the intralayer vibration modes. Raman 29 is also an important probe to investigate interactions in TMDs, such as MoTe₂ and WS₂ ¹³⁻¹⁵, where the strength of the interlayer interaction can be estimated by carefully analyzing the 30 31 splitting. For instance, Davydov splitting is the splitting of bands in the electronic or vibrational

- spectra of crystals due to the breaking of degeneracy by interactions between each subunit (i.e.,
- 2 layer) within the unit cell¹⁶. In addition, Raman spectroscopy is strongly dependent on crystal
- 3 symmetry. Although Raman spectra have been reported previously for WTe₂ thin-layers¹⁷, a full
- 4 understanding of the processes governing thickness-dependent structural transition in WTe₂ is
- 5 still missing.

6

7

2. Methods

- 8 **Experiments:** Atomically thin WTe₂ samples are isolated on SiO₂/Si substrates from
- 9 commercial WTe₂ crystals by the mechanical exfoliation method. The flakes are placed on top of a
- 10 300nm SiO_2/Si substrate and are visible under optical microscope. The thickness of the flakes
- 11 was determined by atomic force microscopy measurements (AFM, Bruker® Nano Dimension
- 12 Edge). The Raman measurements were performed using a Raman spectroscope (Horiba
- 13 JobinYvon® LabRAM HR800) and 532 nm laser with 500 μW power was used as activation light
- source during the measurement.
- **DFT calculations:** First-principles calculations in the framework of density-functional theory¹⁸
- were performed using the Vienna ab initio simulation package (VASP)¹⁹ which employs the
- 17 projector-augmented wave (PAW) method²⁰ for electron-ion interaction. Local-Density
- Approximation (LDA)¹⁸ was adopted for the exchange-correlation potential. Calculations were
- 19 performed using a kinetic energy cutoff of 300 eV. 16 x 8 x 4 and 16 x 8 x 1 Monkhorst-Pack²¹ k-
- 20 point grids were employed to sample the Brillouin of the 3D and 2D unit cells, respectively. For
- 21 the structural optimization, both atoms and cell parameters were relaxed until the residual forces
- reached values smaller than 0.005 eVÅ⁻¹ in absolute values. Phonon modes were calculated using
- 23 the finite displacement method (FDM) in the harmonic approximation provided in the package
- 24 phonopy²². In order to avoid unphysical forces between neighboring atoms due to periodic
- boundary conditions, a $7 \times 7 \times 1$ super-cell was used and has shown to yield well converged
- results for the phonon modes. Raman intensities are calculated in Plazcek approximation²³.

27

28

3. Results and Discussion

- Figure 1(a) shows optical images of 1L to 4L WTe₂ flakes deposited on a SiO₂/Si substrate.
- 30 Each flake in Fig. 1(a) shares the same crystalline orientation since they were exfoliated
- 31 mechanically from the same WTe₂ single crystal and are therefore physically connected to each

other²⁴. The *a* and *b* crystalline axes can be determined by examining the shape of the exfoliated flakes, as marked in Fig. 1(a). The bottom part of Fig. 1(a) shows the height profiles measured by atomic force microscope (AFM), along the red and blue dashed lines drawn on Fig. 1(a). The AFM measurement indicates a step height of a single Te–W–Te atomic layer of about 1.1 nm. The value is slightly larger than the interlayer spacing of ~0.75 nm in the WTe₂ crystals²⁵ and more accurate interlayer spacing can be obtained using the contact mode of AFM²⁶.

7

8

9

10

11

12

13

14

15

16

17

18

19

20

21

22

23

24

25

26

27

28

29

30

31

Figure 1(b) shows the evolution of Raman spectra of the WTe₂ flakes as the thickness varies from one to four layers. Due to the degradation of WTe₂ thin films in ambient conditions, special care has to be taken to protect the samples during the measurements. Specifically, the monolayer is extremely vulnerable to oxidation as shown by the disappearance of characteristic Raman modes after exposure to air for a short time. The measurements were performed by exfoliating and optically characterizing the WTe2 crystals directly in the glove box. The Raman measurements were then carried out immediately after the suitably thin WTe₂ flakes were picked up. Here, we successfully observed seven prominent peaks in the monolayer. We note that the mode centered around ~86.9 cm⁻¹ is found to split into two modes at 82.9 and 89.6 cm⁻¹ in the bilayer. In fact, the observed broad peak at ~86.9cm⁻¹ in the monolayer can also be deconvoluted into two separate peaks as well (as shown in Fig. 1(c)). These two peaks are attributed to Ag and B_g symmetry, respectively. In the following, we will denote all seven peaks at ~85.1, ~88.9, \sim 109.6, \sim 119.4, \sim 135, \sim 164, \sim 216 cm⁻¹ as P1 to P7, respectively. Figure 1(d) exhibits the thickness dependence of the Raman shift for the various Raman active modes from the monolayer to the bulk. Note that in this study the reference, bulk, structure corresponds to a WTe₂ flake featuring 90 layers. The bulk WTe₂ exhibits six Raman modes located at ~79.9, \sim 111.7, \sim 118.0, \sim 133.1, \sim 164.0 and \sim 211.8 cm⁻¹. For consistency with results obtained for single- and bi- layer samples, these modes will be denoted as P1, P3, P4, P5, P6 and P7, respectively. The intensity of the P2 peak gradually fades with an increasing number of layers. We find that only one peak centered at ~ 111.7 cm⁻¹ stiffens as the layer number increases, whereas the P1 (\sim 79.9cm⁻¹), P4 (\sim 118.0cm⁻¹), P5 (\sim 133.1cm⁻¹) and P7 (\sim 211.8cm⁻¹) display a softening trend. Furthermore, the peak at~79.9 cm⁻¹ has the largest shift ($\Delta\omega \approx 5.8$ cm⁻¹) among all the Raman active modes. These features provide a potential fingerprint to determine the number of layers in WTe₂ samples. In contrast, note that the peak at ~ 164 cm⁻¹ remains essentially unaffected by changes in thickness ($\Delta \omega < 0.5 \text{cm}^{-1}$) in the large thickness regime. The 1 reason for this behavior is that the Te atoms belonging to the same plane vibrate in phase in the

P6 vibration mode. Thus the P6 vibration mode (~164 cm⁻¹) is found to be more localized on a

3 layer of WTe₂ and to exhibit weaker or no dependence on thickness^{27, 28}.

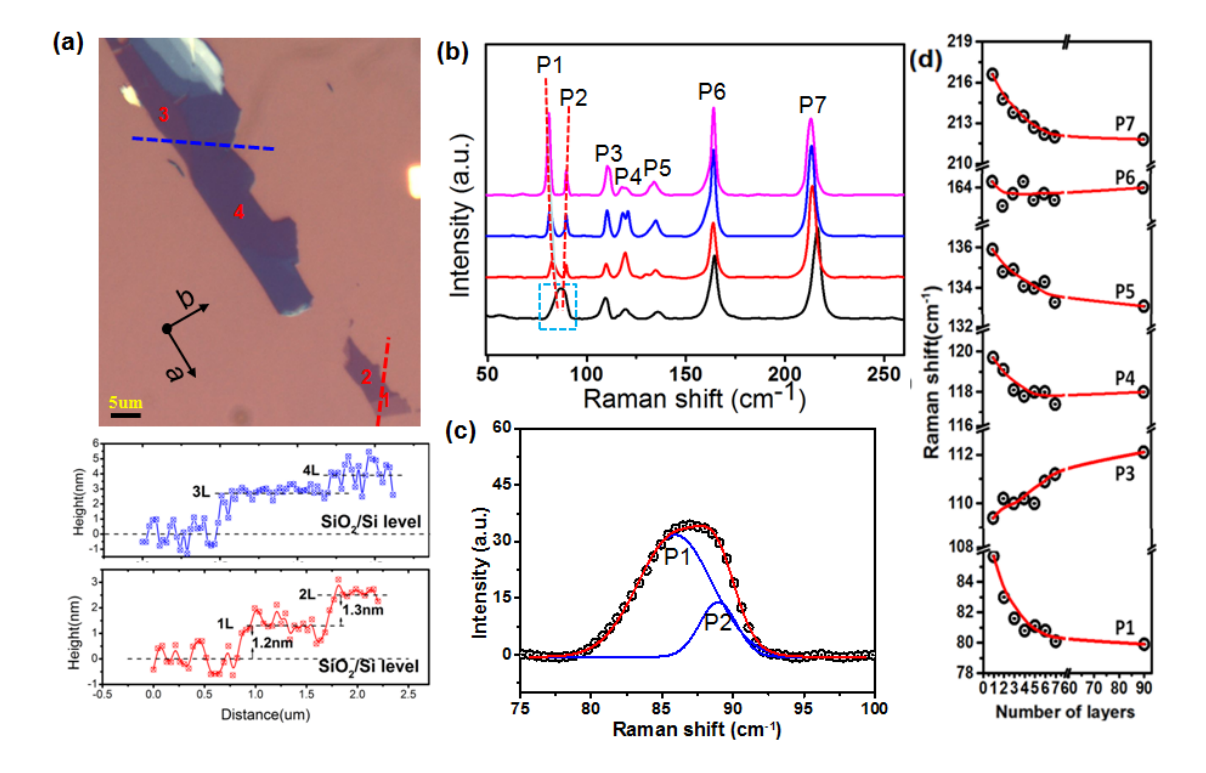


Figure 1: Raman spectra of few layers WTe₂. (a) Optical image of exfoliated WTe₂ flakes deposited on Si/SiO₂ substrate (covered with 300 nm SiO₂). The line profiles measured by AFM shown in the lower part, give the thickness of 1L, 2L, 3L, and 4L. The thickness of the single layer flake measured here is slightly larger than the interlayer spacing of ~0.75 nm found in the WTe₂ crystals. (b) Raman spectra as a function of thickness of WTe₂ varying from 1L to 4L, measured with the excitation wavelength of a 532 nm laser. The spectra are normalized by the intensity of the highest frequency peak. (c) The deconvolution of the (asymmetric) peak centered around ~86.9 cm⁻¹ in the monolayer shows the presence of a split of this mode into two active modes. The dots are experimental data, the blue lines are two Gaussian-fitting profiles and the full width at half maximum (FWHM) of the two separated peaks are about 6.7 and 2.6 cm⁻¹ respectively. (d) The frequency shifts of Raman active modes of WTe₂ plotted as a function of the number of layers clearly show the thickness dependence from monolayer to the bulk.

In addition to the analysis of the normal mode frequency, we performed comparable polarized Raman scattering studies on few layers of WTe₂. Polarized Raman spectroscopy is a powerful method for determining the number of layers and the crystallographic orientation of layered materials. Polarized Raman spectroscopy has been carried out on bulk WTe₂ to assign Raman modes²⁹ and few layers WTe₂³⁰. The measurement is performed by rotating the polarizer clockwise from 0° to 360°. First, zooming onto the 75 - 95 cm⁻¹ frequency range (marked with

blue rectangles in Fig. 1b) for the monolayer WTe₂, we plot the Raman intensities while varying the polarization angles from 0° to 360° (Fig. 2a). The broad Raman peak at 86.9 cm⁻¹ splits into two separate modes, which are attributed to Ag and Bg symmetries (labeled as P1 and P2 in Fig. 1), respectively. When changing the polarization angles, we see that both the P1 and P2 peak intensities change, although the P1 peak intensity shows a stronger dependence on the polarized angle than the P2 peak intensity (Fig. 2c), owing to the different symmetries. Furthermore, the intensity of the P2 peak is much weaker than that of the P1 peak, and thus it is difficult to distinguish them without polarized Raman measurements. We performed a similar polarization analysis for 2L, 3L and 4L, and show only the results of 2L in the right panel of Fig. 2a. For the bilayer WTe₂, the mode around 84 cm⁻¹ (peak P1) can be deconvoluted into two separated modes at 83.5 and 85.2 cm⁻¹ and the separation between the two modes also changes with the polarization angles. Furthermore, an additional mode appears at 89.7 cm⁻¹ (peak P2) as predicted by our DFT calculations (see below). Plotting the Raman frequencies of these observed modes as a function of the number of layers (Fig. 2b) allows us to clearly show the appearance of Davydov splitting with increasing number of layers, as well as the softening of the P1 peak position. The Davydov splitting has been reported for Mo(W)S(Se)₂ previously^{31,32} and it is due to the fact that each layer can vibrate in-phase or 180 degree out-of-phase, causing the splitting starting from 2L. Our results show that the peak P1 and P2 are both observed from 1L all the way to 4L and Davydov splitting of the P1 mode appears after 2L. Furthermore, Davydov splitting of the P2 mode is observed starting from 3L. For 2L, since the split peak has symmetry B2 and has a weak intensity in the back scattering geometry, it can only be resolved at some particular polarization angles. Figure 2(c) compares the polarization dependence of all observed Raman modes. One can

1

2

3

4

5

6

7

8

9

10

11

12

13

14

15

16

17

18

19

20

21

22

23

24

25

26

27

28

29

30

31

Figure 2(c) compares the polarization dependence of all observed Raman modes. One can see that the mode (P1) at \sim 85.1 cm⁻¹ exhibits a 2-lobe shape with the primary polarization directions (for maximum intensity) oriented at about 70° and 250° in the monolayer (marked by a black arrow). We also find that the primary polarization directions of the polar plots rotate clockwise (marked by a blue arrow) to 10° and 190° when the layer number increases to 4L. Such angular dependence of the primary direction on the WTe₂ thickness was also observed for the peaks (P3 \sim P7) centered at \sim 109.6, \sim 119.4, \sim 135, \sim 164, \sim 216 cm⁻¹ in 1L \sim 4L WTe₂. For example, the modes at \sim 135, \sim 164, \sim 216 cm⁻¹ yield a 2-lobe shape with two maximum intensity angles at about 75° and 255°, 30° and 210°, 0° and 180°, 120° and 300° in mono- to four layer

samples, respectively. It is interesting to find that the primary polarization direction rotates clockwise by about 120° with the number of layers increasing from 1L to 4L for almost all observed modes, except for the one (P2) centered at ~89.6 cm⁻¹ for which the peak intensity does not change with the polarization angle. Thus the polarized Raman scattering shows strong angular dependence of Raman intensities of the active modes on the WTe₂ film thickness. Although the angular dependence of active Raman modes have been reported in many 2D materials, such dependence with thickness is here observed for the first time in few layers WTe₂. It is worth noting that similar work by Kim *et. al*³³ reported the 90° rotation of the primary polarization directions between the monolayer and the 2-4 multilayers. The angular dependence of the intensity of the peaks observed here is different from the previously reported results as a different laser polarization set-up was used. In the rest of this manuscript, we establish that our polarized Raman data may reflect the anisotropic nature of a new type of interaction between the layers.

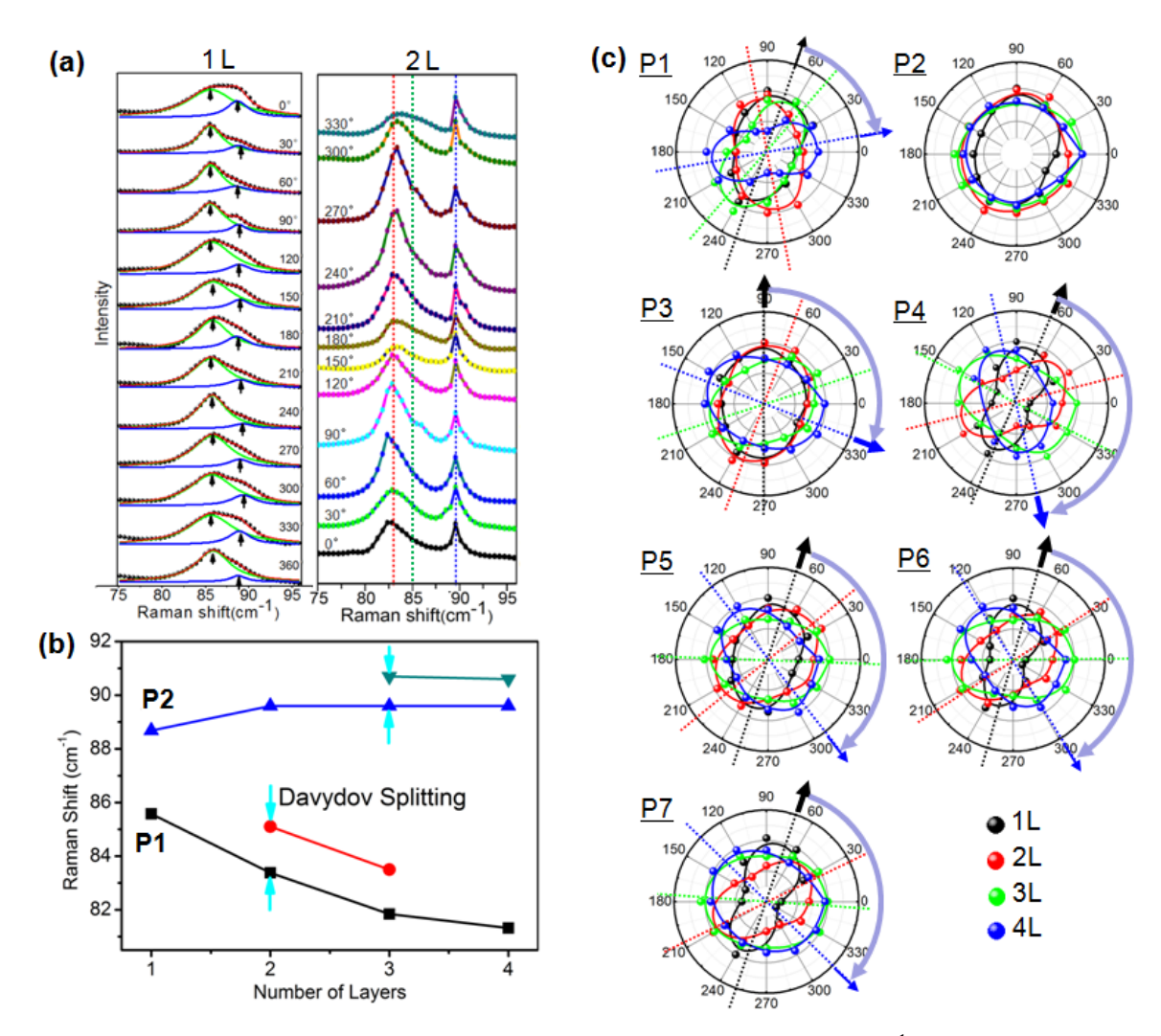


Figure 2: (a) Evolution of Raman peaks in the frequencies between 75—95 cm⁻¹ are shown for

the monolayer and bilayer of WTe₂ as a function of polarization angle. After deconvolution of a broad peak (86.9 cm⁻¹) two separate peaks are resolved. Here, the experimental data are fitted by Lorentzian function (see Fig. 1). (b) The position of the Raman shift of the fitted peaks in the frequencies between 75—95 cm⁻¹ are plotted as the function of the number of layers from 1L to 4L. (c) The dependence of peak intensities with the polarization angle are shown for all the detected modes measured with a 532 nm excitation wavelength. The points in all polar plots are the normalized Raman intensity data and the black and blue arrows mark the primary polarization directions in the 1L and 4L flakes respectively.

DFT calculations

Figure 3a shows the calculated phonon dispersion of the monolayer of WTe₂. The total number of modes is given by 3N, where N is the total number of atoms in the unit cell. The unit cell of the monolayer contains six atoms, resulting in 18 vibrational modes in total. Furthermore, the principle axis of the structure lies along the \vec{b} lattice vector (the structure exhibits a two-fold rotational symmetry with respect to the b-axis) and the atoms are located at the 2e Wyckoff positions³⁴. Therefore, according to the point group C_{2h} (2/m), there are nine Raman active modes in total, six of which belong to the irreducible representation A_g and three belong to the irreducible representation B_g

$$\Gamma^{Raman}_{1L} = 6 \cdot A_g + 3 \cdot B_g .$$

Table 1 provides a summary of the calculated and measured Raman active modes together with their symmetry assignment for monolayer WTe₂. Good agreement is found between calculated and experimental results with a root mean square (rms) relative deviation from experiment of 1.8%. We note the calculated double peak consisting of a mode A_g^6 at 84.6 cm⁻¹ and a B_g^3 mode at 92.5 cm⁻¹. The calculated double peak reproduces the experimental findings (Fig. 1b) as previously reported by Kim et. al³³.

Symmetry	Calculation [cm ⁻¹]	Experiment [cm ⁻¹]			
A_g^6	84.6	85.7			
B_g^3	92.5	88.9			
B_g^2	110.4	109.4			
A_g^5	119.7	119.7			
A_g^4	136.9	135.9			

A_g^3	165.9	164.3
B_g^1	173.7	-
A_g^2	220.5	216.1
A_g^1	221.9	-

Table 1: Calculated and experimentally detected Raman active modes in monolayer WTe₂ with their assigned irreducible representations. We note that the calculated mode at 173 cm⁻¹ is not detected experimentally and the highest frequency modes are predicted to be quasi degenerate.

Adding a second layer of WTe₂ to the monolayer doubles the number of atoms in the unit cell and corresponds to a change in symmetry from the centrosymmetric point group C_{2h} (2/m) to noncentrosymmetric group C_{2v} (mm2). The corresponding phonon band structure is qualitatively very similar to the phonon band structure of single layer WTe₂. The range of vibrational frequencies is the same for mono- and bilayer up to about 250cm⁻¹. In the noncentrosymmetric point group C_{2v} (mm2), all of the possible vibrational modes are Raman active

11
$$\Gamma_{2L}^{Raman} = 12 \cdot A_1 + 6 \cdot A_2 + 6 \cdot B_1 + \frac{12}{2} \cdot B_2 ,$$

where A_1 , A_2 , B_1 and B_2 are the possible irreducible representations of the corresponding space group.

For 3 and 4 layers the number of possible modes grows accordingly, $\Gamma^{Raman}_{3L}=3\cdot\Gamma^{Raman}_{1L}$ and $\Gamma^{Raman}_{4L}=2\cdot\Gamma^{Raman}_{2L}$, but the main features determined by the corresponding point group, such as the possible irreducible representations of modes, remain the same as for mono- and bilayer. The bulk system also has 12 atoms in the unit cell and belongs to the same point group as the structures with even numbers of layers, $\Gamma^{Raman}_{bulk}=\Gamma^{Raman}_{2L}$. We note that the labeling of modes using the irreducible representations is correlated with the reference axis with respect to which the symmetry of the corresponding vibration is analyzed. We also note that the Raman tensors are affected by the choice of the coordinate system. In order to avoid confusion we preserve the irreducible representation labels from the bulk system for the structures with two and four layers and determine the Raman activity by carefully analyzing our calculated Raman tensors and intensities in the back-scattering set-up, which was used experimentally.

Omitting modes with frequencies below 70 cm⁻¹ and the frequencies with B_1 and B_2 symmetry in 2L, 4L and bulk (since those are not detected in back scattering set-up as will be shown below), we compare the remaining calculated frequencies of Raman active modes to the corresponding

experimental values in Table 2. We find an overall good agreement between calculated and measured Raman active modes to be within 2.5% relative rms deviation for 2L, 3.1% for 3L and 2.7% for 4L leading to a 2.8% average relative rms deviation from measured positions. Furthermore, the calculations reproduce the observed Davydov splitting¹⁶ with increasing number of layers, as reflected in the quasi-degeneracy of higher frequency modes with increasing number of layers. This type of splitting is also responsible for the appearance of multiple peaks in the region extending from 70 cm⁻¹ to 95 cm⁻¹ for 2L, 3L and 4L structures, as also measured experimentally (see Fig. 2). We also observe the mode softening of the lowest A1(Ag) mode from 84.6 cm⁻¹ in 1L (Tab. 1) over 77.9 cm⁻¹ in 2L and to 72.7 cm⁻¹ in bulk, resulting in a total frequency change of about 12 cm⁻¹. The second mode in 1L at 92.5 cm⁻¹ (Tab. 1) softens as well although much less with only 3.4 cm⁻¹ overall softening from 1L to bulk. Such mode softening and "spreading" of the distance between the two peaks in the original double peak in 1L was already reported experimentally by Kim et. al³³. In addition, our calculations also predict appearance of additional peaks for 3L and 4L in the region between the two peaks. This additional splitting is theoretically predicted (Fig. 3c) and experimentally reported (Fig. 2b) here for the first time. For higher frequency modes our calculations also predict the presence of multiple peaks. However, due to the very small frequency difference between those modes, they are likely to remain unresolved in experiment.

1

2

3

4

5

6

7

8

9

10

11

12

13

14

15

16

17

18

2L			3L			4L			Bulk		
Sym.	CAL.	EXP.									
			Ag	73.9	81.6	A1	74.4	80.8	A1	72.7	79.9
A1	77.9	83.0	Ag	84.4	-	A1	82.9	-			
A2	91.7	89.6	Ag	88.0	87.7	A2	90.5	89.7	A2	89.1	-
			Bg	91.2	89.7	A2	91.7	90.6			
A2	111.2	110.2	Bg	111.3	110	A2	111.6	110.2			
			Bg	113.8	111	A2	114.7	111.5			
A2	118.0	-	Bg	116.7	-	A1	115.7	117.8	A1	114.6	111.7
A1	118.3	119.4	Ag	118.4	118.1	A2	117.2	-	A2	115.8	-
			Ag	120.9	120.9	A1	118.8	120.1			
			Ag	131.6	-	A2	119.6	-	A2	118.3	118.0
			Ag	132.5	-	A1	126.8	-			
A1	129.9	130.0	Ag	133.2	132.2	A1	130.4	-	A1	130.3	-
A1	132.0	-				A1	131.9	131.7			
A1	133.6	134.8	Ag	135.2	134.9	A1	133.1	-	A1	133.5	133.1
						A1	133.5	134.1			

						A1	135.7	-	A1	135.9	-
A2	158.8	-	Bg	158.7	-	A2	158.1	-	A2	159.0	-
			Ag	161.5	160.8	A2	159.6	-			
			Bg	162.7	-	A1	162.4	160.9	A1	163.8	164.0
A1	164.7	163.7	Ag	165.1	163.9	A1	164.6	164.1			
A2	169.2	-	Bg	168.8	-	A2	166.9	-	A2	164.7	-
A1	181.2	-	Ag	181.0	-	A2	170.3	-			
						A1	180.0	-	A1	180.3	-
			Ag	211.7	-	A1	181.7	-			
A1	216.7	213.3	Ag	216.5	212.4	A1	207.8	211.8	A1	209.4	-
A1	219.3	214.8	Ag	217.9	213.8	A1	215.9	213.5	A1	215.7	211.8
			Ag	220.4	-	A1	217.5	-			
						A1	219.2	-			
A1	243.5	-	Ag	243.4	-	A1	238.1	-	A1	239.3	-
						A1	243.4	-			

Table 2: Calculated and experimental Raman active modes in 2 to 4 layer WTe₂ and bulk with
 their assigned irreducible representations.

3

4

5

6

7

We now turn to the symmetry analysis of modes based on investigating their polarization dependence profiles. From the theoretical point of view, the Raman intensity as computed within the Plazcek approximation is proportional to the square of the absolute value of the inner product between the polarization vectors of incident and scattered light \vec{e}_i and \vec{e}_s and the Raman tensor \tilde{R} of the mode in question

$$I \propto |\vec{e}_S \cdot \tilde{R} \cdot \vec{e}_i|^2 . \tag{1}$$

The matrix elements of the (3×3) symmetric Raman tensor of the j-th phonon mode for incident laser energy E_L are given by 35,36

11
$$\tilde{R}_{\alpha\beta}(j, E_L) \propto \sqrt{\frac{1}{\omega_j}} \sum_{\mu=1}^{N} \sum_{i=1}^{3} \frac{\partial \varepsilon_{\alpha\beta}(v_L) e_i^j(\mu)}{\partial r_i(\mu) \sqrt{M_{\mu}}}, \qquad (2)$$

where $\varepsilon_{\alpha\beta}(v_L)$ is the complex dielectric tensor at the laser frequency v_L , $r_i(\mu)$ is the position of the μ -th atom along the i-th direction (i=x,y,z). Furthermore, $\frac{e_i^i(\mu)}{\sqrt{M_\mu}}$ is the displacement of the μ -th atom with mass M along the i-th direction in the j-th phonon mode with frequency ω_j . For simulations of non-resonant Raman scattering it is common practice to consider only the static dielectric tensor $\varepsilon_{\alpha\beta}(v_L=0)$ and neglect the dependence of ε on the frequency of the incident laser. Here, in contrast, we compute $\varepsilon_{\alpha\beta}(v_L)$ for the experimentally given frequency of the laser light with the goal of capturing resonance effects in first-order Raman scattering 37 .

Figure 3(c) shows the calculated Raman spectra for 1L to 4L and bulk for the energy of the incident light of 2.33 eV, which corresponds to the wavelength of 532 nm used experimentally. A back-scattering set-up is assumed and the polarization of the incident light is at 0°. Here, we present results corresponding to an averaging over the polarization of the scattered light. The Raman spectra calculated based on Eq. 2 clearly reflect the features discussed on the basis of the results shown in Tab. 2 and therefore support the Raman activity of the discussed modes by showing the non-vanishing intensity of the corresponding modes. More importantly, our DFT calculations reproduce that the A1(Ag) and A2(Bg) modes between 75~95 cm⁻¹ exist in few layers of WTe₂, including the evolution of Raman shifts of these modes with the number of layers. In addition, as mentioned above, our calculations also predict the Davydov splitting and its thickness dependence. In order to better illustrate this, we present vibration patterns of the Raman modes A1(Ag) and A2(Bg) observed in the monolayer, where the A1(Ag) mode further splits due to the Davydov splitting in the bilayers in Fig. 3(b). As we see, the A1(Ag) mode includes the out-of-plane vibration and is softened when the number of layers increases. In contrast, the A2(Bg) mode is an in-plane vibration and almost not shifted by increasing layers.

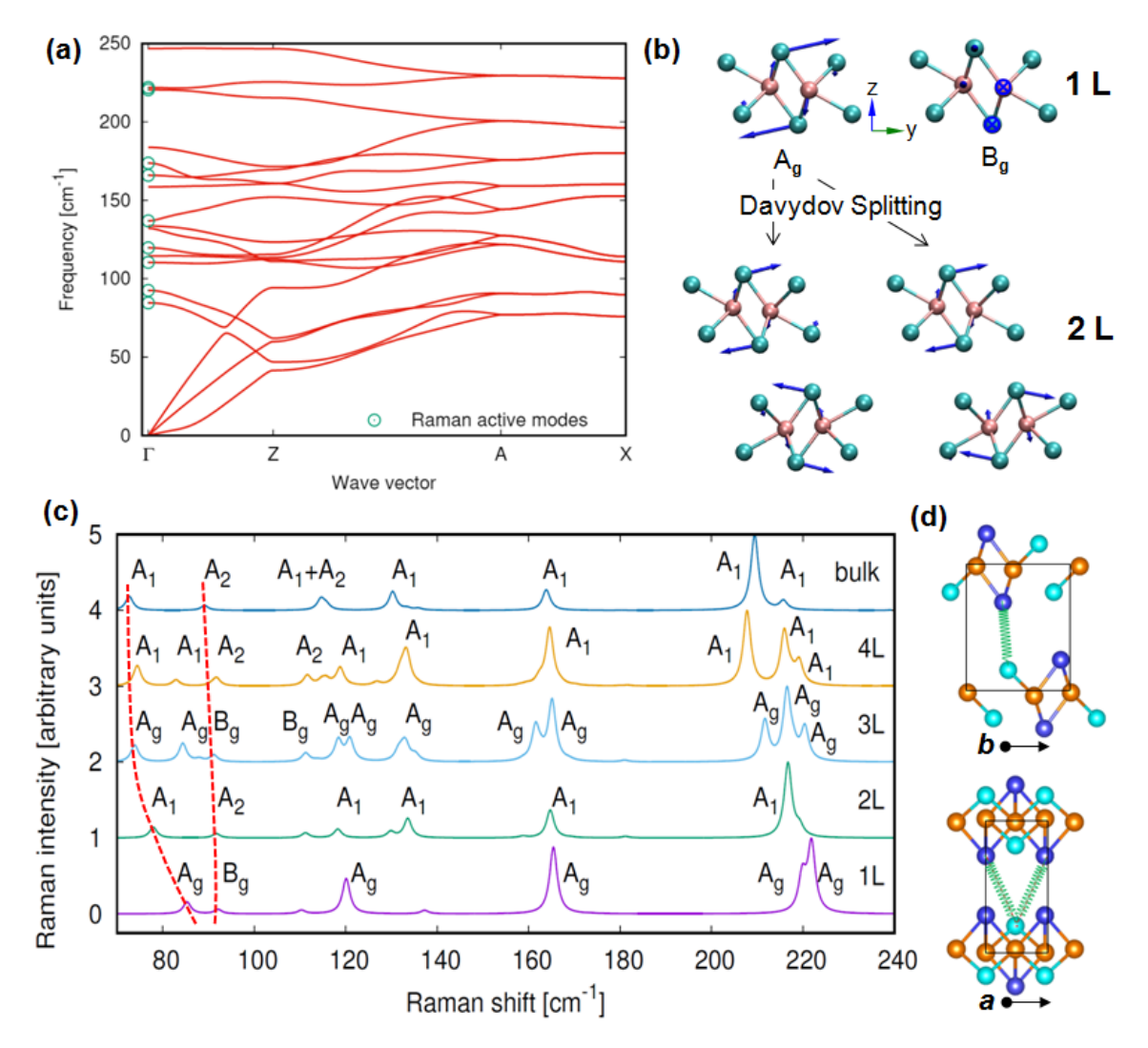


Figure 3: (a) Calculated phonon dispersion relation of monolayer WTe₂ in the corresponding first Brillouin zone. The green circles mark the Raman active modes in monolayer WTe₂ and the phonon symmetries are A_g^6 (84.6 cm⁻¹), B_g^3 (92.5 cm⁻¹), B_g^2 (110.4 cm⁻¹), A_g^5 (119.7 cm⁻¹), A_g^4 (136.9 cm⁻¹), A_g^3 (165.9 cm⁻¹), B_g^1 (173.7 cm⁻¹), A_g^2 (220.5 cm⁻¹), A_g^1 (221.9 cm⁻¹) accordingly. (b) Vibration patterns of the Raman modes A1 (A_g) and A2 (B_g) observed in the monolayer. For the bilayer, the A1(A_g) mode further splits into two modes, as shown underneath, due to the Davydov splitting. (c) Calculated evolution of Raman spectra from 1L to 4L and bulk for the laser wavelength of 532 nm in a back-scattering set-up. The polarization angle of the incident light is set to 0°, and the polarization of the scattered light is averaged. (d) Schematic illustration of the directional interlayer interactions due to the interlayer electronic hybridization. Green springs are cartoons to represent the directional binding between Te atoms in adjacent layers.

We now turn our attention to the angular dependence of polarization Raman spectra. The Raman tensors for modes with irreducible representations A_g and B_g in the centrosymmetric point group C2h (2/m) are given by³⁸

$$\tilde{R}(A_g) = \begin{pmatrix} b & 0 & d \\ 0 & c & 0 \\ d & 0 & a \end{pmatrix}, \quad \tilde{R}(B_g) = \begin{pmatrix} 0 & f & 0 \\ f & 0 & e \\ 0 & e & 0 \end{pmatrix}$$
 (3)

1 and by

9

10

11

12

13

14

15

16

17

21

22

$$2 \qquad \tilde{R}(A_1) = \begin{pmatrix} a & 0 & 0 \\ 0 & b & 0 \\ 0 & 0 & c \end{pmatrix}, \tilde{R}(A_2) = \begin{pmatrix} 0 & d & 0 \\ d & 0 & 0 \\ 0 & 0 & 0 \end{pmatrix}, \tilde{R}(B_1) = \begin{pmatrix} 0 & 0 & e \\ 0 & 0 & 0 \\ e & 0 & 0 \end{pmatrix}, \tilde{R}(B_2) = \begin{pmatrix} 0 & 0 & 0 \\ 0 & 0 & f \\ 0 & f & 0 \end{pmatrix}$$
 (4)

for the modes with irreducible representations A_1 , A_2 , B_1 , and B_2 in the noncentrosymmetric point group C2v (mm2). Note, while the individual tensor elements have different numerical values in the two point groups, the same letters are used for convenience. We also note the close relation of the Raman tensors in the two distinct point groups: The Raman tensor for the A_g mode has the structure of the sum of $\tilde{R}(A_1)$ and $\tilde{R}(B_1)$, while $\tilde{R}(B_g)$ resembles the sum of $\tilde{R}(A_2)$ and $\tilde{R}(B_2)$.

In a back-scattering set-up, the polarization vectors lie in the ab-plane of the crystal and for the case of linear polarization of the laser light are given by $\vec{e}_i = (\cos \theta, \sin \theta, 0)$ and $\vec{e}_s = (\cos \gamma, \sin \gamma, 0)$. Thus, the intensity (eq. 1) of modes belonging to the B_1 and B_2 irreducible representations vanishes—in the back-scattering set-up and such modes are not detected. This leaves the modes of types A_g and A_g and A_g and A_g detectable in the particular experimental set-up. However, since all contributions to the intensity from the Raman tensor elements associated with the c-direction of the structure are now suppressed by the choice of the direction of the laser polarization, the effective Raman tensors are the same for modes A_g and A_g , and A_g , respectively. It follows that those modes will have the same qualitative polarization dependence profile. Specifically,

18
$$I(A_g) \propto |b\cos\theta\cos\gamma + c\sin\theta\sin\gamma|^2 ,$$

19
$$I(B_q) \propto |f\cos\theta\sin\gamma + f\sin\theta\cos\gamma|^2 , \qquad (5)$$

and identical expressions, except for different numerical values for b, c, f, are found for $I(A_1)$ and

 $I(A_2)$, respectively. When no specific polarization setup is selected for the scattered light, i. e. a

mixing of all possible polarizations is used, the resulting intensity is averaged over the angle of

23 the polarization of the scattered light γ over the interval $[0, 2\pi]$.

24 Hence, we find the polarization dependence profiles of the average intensity of modes A_g and A₁

25 and B_g and A_2 to be

26
$$\overline{I}(A_g) \propto \overline{I}(A_1) \propto \cos^2 \theta + r^2 \sin^2 \theta ,$$
27
$$\overline{I}(B_g) \propto \overline{I}(A_2) \propto |f|^2 = constant , \qquad (6)$$

with $r^2 = \left| \frac{c}{b} \right|^2$. The intensity of modes of type A_g and A_1 will therefore show a dependence on the 1 2 polarization angle θ which can either have the shape of a perfect circle for r = 1 or, for r > 1, the shape of the number eight with decreasing "waist width" for growing r. In contrast, since the 3 4 intensity of modes of type B_g and A_2 does not depend on θ , their polarization profile will always exhibit a circular shape. We note here, that the Raman tensor elements a and b will typically be 5 6 different from each other leading to distinguishable polarization profiles for modes of type A1 7 (Ag) and A2 (Bg). 8 By fitting the experimental data from the polarization dependence profiles in Fig. 2c to the 9 theoretically predicted ones described by Eqs. 5-6, we are able to analyze the symmetry of the 10 experimentally detected modes. We find good agreement with the calculated symmetry modes if 11 we take into account the experimental uncertainty and the fact that whenever there are two or 12 more modes of different symmetries (e. g., A1(Ag) and A2(Bg)) having very similar frequencies (Tab. 2), the polarization dependence profile of a experimentally detected single peak will behave 13 14 as some kind of superposition of the two polarization profiles given by Eq. 5. This effect is 15 illustrated in the case of the "hidden" double peak in 1L as well as for the higher lying mode at 16 about 164 cm⁻¹ starting from 2L. 17 The angular polarization dependence on the thickness for few layers of WTe2 observed here, first reflects crystalline lattice symmetries of few-layers 2D materials. However, as mentioned 18 before, these WTe2 flakes share the same crystalline orientation since they were exfoliated 19 20 mechanically from the same single crystal and are physically connected. Therefore, the observed rotation of the primary polarization directions with the thickness reflects that the existence of 21 22 directional interlayer interactions, instead of van der Waals couplings, playing the essential role in affecting the phonon modes, especially in anisotropic 2D materials WTe2. It is worth noting 23 24 that the primary polarization directions rotates clockwise about 120° with the number of layers 25 increasing from 1L to 4L for almost all observed modes. The primary polarization of each Raman modes rotates roughly about 45° with every additional layer going from 1L to 4L. 26 A reasonable explanation for the results presented before is the existence of interactions that 27 28 are stronger that simple van der Waals forces., as it has already been reported in several other 2D materials such as PtS₂³⁹/PtSe₂⁴⁰ and BP (black phosphorus)^{41, 42}. This is a highly directional 29 interlayer interaction, different from vdW interactions, arising from the electronic hybridization 30

of the lone electron-pairs and an appreciable amount of overlap between electronic densities centered on each individual layer. In 2D materials such as multilayer graphene and h-BN, the primary interlayer coupling is *vdW* forces, which generally have only weak effects on intra-layer (optical) vibration modes. However, in the case of BP, P atom bonds with three neighboring P atoms and has one lone pair of electrons on each atom that is orientated out of the layer. In WTe₂ distorted structure there is also strong electronic hybridization between Te atoms in WTe2 giving rise to interlayer coupling beyond simple *vdW* interaction. To better illustrate these interlayer interactions, we visualize such interaction as a spring connecting two adjacent layers, as shown in Fig. 3d. Such interaction induces a directional interaction which affects both interlayer (shear and breathing) and intralayer phonons modes and eventually accounts for the observed angular polarization dependence with the thickness. Moving from the analysis of individual mode, we will now further demonstrate how Raman spectra can be used to identify layer thickness in a mixed sample. To this end, we performed a spatial Raman mapping of a sample featuring various numbers of layers. Figure 4a shows the optical images of mono- to multi-layers WTe2 on Si substrate with 300 nm SiO2 layer. We determined the thickness of WTe2 samples, by combining the means of optical microscopy and the tapping mode AFM. Figure 4b shows Raman intensity maps for all 6 modes measured in the red dotted region in Fig. 4a. To generate the peak intensity maps, Raman spectra at points that form a rectangular array of dimension 0.5 μm x 0.7 μm are collected. The intensity of a Raman mode at each point was calculated by the average signal intensity over the corresponding peak dispersion range. All 6 modes have the weakest Raman signals in the monolayer region. This may be due to the fact that mono- and bilayer WTe2 are very susceptible to atmospheric corrosion. In addition, the intensity maps of the P1, P3 and P7 modes are comparable to the red dotted region in Fig. 4a and they all have strongest Raman scattering in the four-layer region. We also find that the intensity maps of the P4, P5 and P6 modes are less consistent with the AFM image. We postulate that this may be due to the presence of defects in the WTe2 materials or surface adsorbents such as O2 and H2O. These three Raman modes are more sensitive to oxidation or surface adsorbents and cannot be used as the reliable fingerprint for determination of the thickness.

1

2

3

4

5

6

7

8

9

10

11

12

13

14

15

16

17

18

19

20

21

22

23

24

25

26

27

28

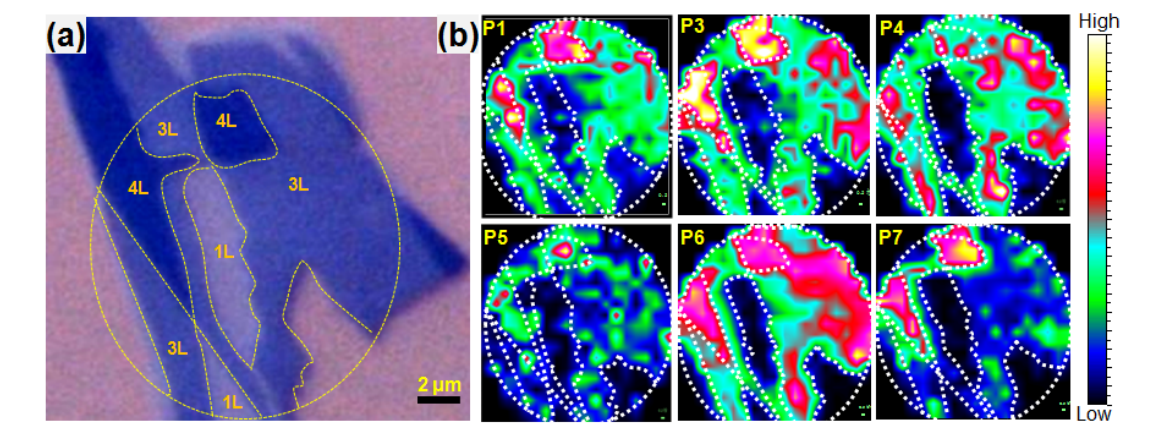


Figure 4: (a) Optical microscopic images of mono- to multilayer WTe_2 on Si substrate with 300 nm SiO_2 layer. (b) Raman intensity maps for all 6 modes measured in the yellow dotted region in Fig. 4a.

4. Conclusion

In summary, we have performed a comprehensive and systematic investigation of few layers WTe $_2$ flakes by combining Raman scattering and DFT calculations. We observed Raman signatures corresponding to the structure transition from noncentrosymetric T_d to centrosymetric phases occurring when the thickness is scaled down from bilayer to monolayer. Furthermore, we showed that the polarized Raman scattering features strong angular dependence on the WTe $_2$ film thickness. In particular, our combined experimental/theoretical study resolves the mode splitting using the polarized Raman. DFT calculations reproduce the experimental results, including the presence of the A1(A $_g$) and A2(B $_g$) modes located between 75~95cm $^{-1}$ in few-layer samples from 1L to 4L. Our results show that high-quality Raman spectra can be used not only as a reliable fingerprint for the determination of the thickness and the crystallographic orientation, but also as probes for the relatively strong directional interlayer interactions in few layers of WTe $_2$.

References and Notes

Acknowledgements

This work was conducted at the analysis and test center and the Department of Physics of Huazhong University of Science and Technology in China. HY and MHP acknowledge the financial supported by National Natural Science Foundation of China (Project Code 11574095). Work at Rensselaer Polytechnic Institute (N. S. and V. M.) was supported by NSF Grant EFRI 2-DARE

- 1 (EFRI-1542707). A portion of this research (Raman scattering modeling) used resources at the
- 2 Center for Nanophase Materials Sciences, which is a DOE Office of Science User Facility operated
- 3 by the Oak Ridge National Laboratory. L. L. was supported by Eugene P. Wigner Fellowship at the
- 4 Oak Ridge National Laboratory and by the Center for Nanophase Materials Sciences.

5

6 **Author contributions**

- 7 C. Y and HY performed Raman measurements. N. S., L. L. and V. M. carried out the theoretical
- 8 analysis. All authors discussed the results and contributed to writing the manuscript.

9

10

Additional Information

- 11 **Supplementary Information** accompanies this paper at
- 12 **Competing financial interests:** The authors declare no competing financial interests.
- 13 **Reprints and permission** information is available online at XXX.

14 15

References

- 16 [1] Lee, C. et al. Anomalous Lattice Vibrations of Single- and Few-Layer MoS₂. *Acs Nano* **4**, 2695-2700 (2010).
- 18 [2] Li, H. et al. From Bulk to Monolayer MoS₂: Evolution of Raman Scattering. *Advanced Functional Materials* 22, 1385-1390 (2012).
- 20 [3] Yamamoto, M. et al. Strong Enhancement of Raman Scattering from a Bulk-Inactive Vibrational Mode in Few-Layer MoTe₂. *Acs Nano* **8** (2014).
- 22 [4] Mak, K.F., Lee, C., Hone, J., Shan, J. & Heinz, T.F. Atomically thin MoS₂: A New Direct-Gap Semiconductor. *Physical Review Letters* **105**, 136805 (2010).
- 24 [5] Splendiani, A. et al. Emerging photoluminescence in monolayer MoS₂. Nano Letters 10, 1271 (2010).
- [6] Xi, X. et al. Strongly enhanced charge-density-wave order in monolayer NbSe₂. Nature
 Nanotechnology 10, 765 (2015).
- 27 [7] Ali, M.N. et al. Large, non-saturating magnetoresistance in WTe₂. Nature 514, 205-8 (2014).
- 28 [8] Das, P.K. et al. Layer-dependent quantum cooperation of electron and hole states in the anomalous semimetal WTe₂. *Nature Communications* 7, 10847 (2016).
- Jiang, J. et al. Signature of Strong Spin-Orbital Coupling in the Large Nonsaturating Magnetoresistance
 Material WTe₂. *Phys Rev Lett* 115, 166601 (2015).
- 32 [10] Soluyanov, A. et al. Type-II Weyl semimetals. *Nature* **527**, 495 (2015).
- 33 [11] Brown, B.E. The crystal structures of WTe₂ and high-temperature MoTe₂. *Acta Crystallographica* **20**, 268–274 (1966).
- 35 [12] Ferrari, A.C. & Basko, D.M. Raman spectroscopy as a versatile tool for studying the properties of graphene. *Nature Nanotechnology* **8**, 235-246 (2013).
- 37 [13] Froehlicher, G. et al. Unified Description of the Optical Phonon Modes in N-Layer MoTe₂. *Nano* 38 *Letters* 15, 6481 (2015).
- 39 [14] Song, Q.J. et al. Physical origin of Davydov splitting and resonant Raman spectroscopy of Davydov

- 1 components in multilayer MoTe₂. *Phys.rev.b* **93**, 115409 (2016).
- 2 [15] Staiger, M. et al. Splitting of the monolayer out-of-plane A'₁ Raman mode in few-layer WS₂. *Physics* **91** (2015).
- 4 [16] Davydov, A.S. Reviews of Topical Problems: the Theory of Molecular Excitons. *Soviet Physics*5 *Uspekhi* **31**, 145-178 (1964).
- 6 [17] Jiang, Y.C., Gao, J. & Wang, L. Raman fingerprint for semi-metal WTe₂ evolving from bulk to monolayer. *Scientific Reports* 6 (2016).
- 8 [18] Kohn, W. & Sham, L.J. Self-consistent equations including exchange and correlation effects. *Physical Review* **140**, A1133-A1138 (1965).
- 10 [19] Furthmüller, J. and Kresse, G. K. Efficient iterative schemes for ab initio total-energy calculations using a plane-wave basis set. *Physical Review B* **54** 11169 (1999).
- 12 [20] Blöchl, P.E. Projector augmented-wave method. *Physical Review B* 50, 17953-17979 (1994).
- [21] Monkhorst, H.J. & Pack, J.D. Special points for Brillouin-zone integrations. *Physical Review B* 13, 5188-5192 (1976).
- [22] Togo, A. & Tanaka, I. First principles phonon calculations in materials science. *Scripta Materialia* 108,
 1-5 (2015).
- 17 [23] Placzek, G. The Rayleigh and Raman Scattering. UCRL trans 526 (1959).
- [24] Ling, X. et al. Anisotropic Electron-Photon and Electron-Phonon Interactions in Black Phosphorus.
 Nano Letters 16, 2260 (2016).
- [25] Bullett, W.G.D.a.D.W. Electronic structure and crystallography of MoTe₂ and WTe₂. *J. Phys. C: Solid* State Phys. 20 (1987).
- [26] Nemes-Incze, P., Osváth, Z., Kamarás, K. & Biró, L.P. Anomalies in thickness measurements of
 graphene and few layer graphite crystals by tapping mode atomic force microscopy. *Carbon* 46, 1435 1442 (2008).
- 25 [27] Lee, J. et al. Single- and few-layer WTe₂ and their suspended nanostructures: Raman signatures and nanomechanical resonances. *Nanoscale* **8**, 7854-60 (2016).
- [28] Jana, M.K. et al. A combined experimental and theoretical study of the structural, electronic and vibrational properties of bulk and few-layer Td-WTe₂. Journal of Physics Condensed Matter An Institute of Physics Journal 27, 285401 (2015).
- [29] Kong, W.D. et al. Raman scattering investigation of large positive magnetoresistance material WTe₂.
 Applied Physics Letters 106, 205 (2015).
- 32 [30] Qingjun Song, H.W.et al. The polarization-dependent anisotropic Raman response of few-layer and bulk WTe₂ under different excitation wavelengths. *RSC Adv.* **6** (2016).
- 34 [31] Philipp Tonndorf, R.S.et al. Photoluminescence emission and Raman response of monolayer MoS₂, 35 MoSe₂, and WSe₂. *OPTICS EXPRESS* **21** (2013).
- [32] Terrones, H. et al. New first order Raman-active modes in few layered transition metal dichalcogenides.
 Sci Rep 4, 4215 (2014).
- 38 [33] Kim, M. et al. Determination of the thickness and orientation of few-layer tungsten ditelluride using polarized Raman spectroscopy. *2D Materials* **3** (2016).
- 40 [34] Determination of the Wyckoff positions is provided as part of the symmetry analysis feature in the phonopy software
- 42 [35] Liang, L. & Meunier, V. First-principles Raman spectra of MoS₂, WS₂ and their heterostructures. 43 *Nanoscale* **6**, 5394-401 (2014).
- 44 [36] Umari, P., Pasquarello, A. & Dal Corso, A. Raman scattering intensities in alpha-quartz: A first-principles investigation. *Physical Review B* **63**, 094305 (2001).
- 46 [37] Talirz, L. et al. On-Surface Synthesis and Characterization of 9-Atom Wide Armchair Graphene

- 1 Nanoribbons. ACS Nano 11, 1380-1388 (2017).
- [38] Kroumova, E. et al. Bilbao Crystallographic Server: Useful Databases and Tools for Phase-Transition
 Studies. *Phase Transitions* 76, 155-170 (2003).
- 4 [39] Zhao, Y. et al. Extraordinarily Strong Interlayer Interaction in 2D Layered PtS₂. *Adv Mater* **28**, 2399-5 407 (2016).
- 6 [40] Zhao, Y. et al. High-Electron-Mobility and Air-Stable 2D Layered PtSe₂ FETs. *Adv Mater* **29** (2017).
- [41] Hu, Z.X., Kong, X., Qiao, J., Normand, B. & Ji, W. Interlayer electronic hybridization leads to exceptional thickness-dependent vibrational properties in few-layer black phosphorus. *Nanoscale* 8, 2740 (2015).
- [42] Jingsi Qiao, X.K., Zhi-Xin Hu, Feng Yang and Wei Ji. High-mobility transport anisotropy and linear
 dichroism in few-layer black phosphorus. *Nature Communications* (2014).